Hindawi
International Journal of Rotating Machinery
Volume 2022, Article ID 9913692, 14 pages
https://doi.org/10.1155/2022/9913692

Research Article

Experimental and Numerical Studies of the Film Cooling Effectiveness Downstream of a Curved Diffusion Film Cooling Hole

Fan Yang and Mohammad E. Taslim

Mechanical and Industrial Engineering Department, Northeastern University, Boston, Massachusetts 02115, USA

Correspondence should be addressed to Mohammad E. Taslim; m.taslim@neu.edu

Received 30 January 2022; Revised 16 March 2022; Accepted 25 March 2022; Published 9 May 2022

Academic Editor: Jechin Han

Copyright © 2022 Fan Yang and Mohammad E. Taslim. This is an open access article distributed under the Creative Commons Attribution License, which permits unrestricted use, distribution, and reproduction in any medium, provided the original work is properly cited.

Film cooling technology is a commonly used method for thermal protection of gas turbines' hot sections. A new, shaped, film cooling hole is proposed in this study. The geometry is made of a straight-through cylindrical feed hole at an inclination angle of 30° followed by an expansion section. The expansion section is created by the rotation of the same circular hole on the inclination plane about an axis normal to that plane which passes through the center of the feed hole exit area. This shape was designed to decrease the deteriorating effects of kidney vortices by proper distribution of the coolant flow emerging from the hole exit area. Cases with four rotation angles (7°, 14°, 17.5°, and 21°) were studied both experimentally and numerically and for the blowing ratios of 0.5, 1, and 2.0. For comparisons, the commonly used 7°-7°-7° diffusion hole geometry was also tested under otherwise identical conditions. For data collection, the pressure-sensitive paint (PSP) technique was used to measure the film cooling effectiveness. Streamwise- and spanwise-averaged film effectiveness results were obtained to compare the performance of different geometries. The main conclusions were that the case of 21° rotation angle produced the highest film effectiveness and outperformed the 7°-7°-7° diffusion hole geometry.

1. Introduction

Gas turbines are widely used in industry and military fields. To satisfy the increasing demand for turbine efficiency and power output, the temperature of gases in the combustion chamber is being increased continuously. Film cooling is an external method used in gas turbines to protect the components that are exposed to hot gases. The main idea is to introduce a secondary fluid from discrete film holes to the surface of components. The coolant forms a thin layer that covers the downstream region to prevent it from contacting hot gases. The goal is to obtain the maximum coolant coverage with the minimum aerodynamic losses.

Film cooling studies began as early as 1960 [1]. Hartnett et al. [2] studied the tangential injection and collected the heat transfer data at the conditions of both adiabatic and constant heat flux walls. Goldstein [3] presented a review that summarized the early film cooling geometries and research. Basic geometries like tangential injection layers, reverse coolant injection, and angled slots can be found in his study. Over the years, researchers [4–14] have improved the effectiveness by continuously developing different geometries. Bunker [15] summarized the literature on shaped hole film cooling over 30 years. He pointed out that the shaped holes have low sensitivity to mainstream turbulence intensity variations. And the greatest advantage of most shaped holes is that the effectiveness is increasing with the blowing ratio. However, the formation of kidney vortices is always a problem that prevents the coolant from attaching to the target surface.

Anti-kidney-vortex geometries have been under investigation as early as 1997 by Haven et al. [16]. Double-jet and sister-hole geometries have been investigated during the past decade [17–22]. Recently, Zhou et al. [23], Yao et al. [24], and Zhu et al. [25] have studied the effects of the diameter ratio of the side hole and main hole on film cooling effectiveness in double-jet and tripod holes. The interaction between

the upstream and downstream film cooling rows was the subject of investigation by Wang et al. [26] who concluded that such interaction weakens the effects of the kidney vortices. Some related US patents have also been registered by researchers in this area [27–29]. In this study, a diffusion hole is proposed that can be envisioned as a passage that can be created by the rotation of a circular hole about the axis z in Figures 1 and 2, normal to the film-cooled surface, and passes through the center of the metering hole cross-section. With today's laser drilling technology, these holes are easily producible. With rotation angle $\theta > 15^\circ$, these film hole geometries are believed to diminish the effects of kidney vortices without the help of any side holes. Each film hole starts with a circular metering hole, extending to about half of the wall thickness, and then expands laterally as shown in Figure 1. Due to the film hole curved exit area, the coolant velocity profile has its maximum along the axis of the hole exit area and decreases to a minimum close to the spanwise edges; thus, there is not a strong interaction between the coolant and the main (hot) flow around those edges resulting in no kidney vortices beyond a threshold value of the rotation angle, θ. Four cases, all with an inclination angle of $\alpha = 30^\circ$ and four rotation angles, $\theta = 7^\circ$, 14°, 17.5°, and 21°, shown in Figures 2 and 3, are studied at the blowing ratios of 0.5, 1, and 2. The conventional 7°-7°-7° diffusion hole is used as the baseline case to which the results of these proposed film hole geometries are compared.

In the experimental part, the pressure-sensitive paint method, a proven technique, was used to measure film effectiveness. Using pure nitrogen gas as the coolant and air as the main (gas) flow, both at ambient conditions, the density ratio was close to 0.97.

2. Experimental Setup

Figure 4 shows the schematics of the test rig representing the air and nitrogen plenums as well as the removable test piece on which different film hole geometries were machined using a five-axis numerically controlled milling machine. Air and nitrogen plenums were fabricated with 0.127 cm thick clear acrylic plastic slabs. Each plenum was equipped with a honeycomb flow straightener to send a uniform flow to the main channel and the film holes. Air entered the main channel from the big plenum through a bellmouth opening.

As shown in Figure 5, a 100 psi rotary-vane air compressor supplied the main flow corresponding to a Reynolds number of 87,200. An air dryer was connected to the compressor to remove the water vapor. Two cartridge filters were used to remove any residual water vapor from the air flow. The coolant was supplied by a commercially available nitrogen tank. Critical Venturi meters, choked at all inlet flow conditions, and precision pressure dials were used to control and measure the mass flow rates of air and nitrogen. K-type thermocouples were inserted through small holes into the test section and pipes to measure the flow temperatures using a temperature acquisition system. The removable test plate with three film holes was placed on the nitrogen plenum, flushed with the main channel bottom surface during each test. The reported data in all geometries are for the middle hole to eliminate any side effects. A 400 nm UV

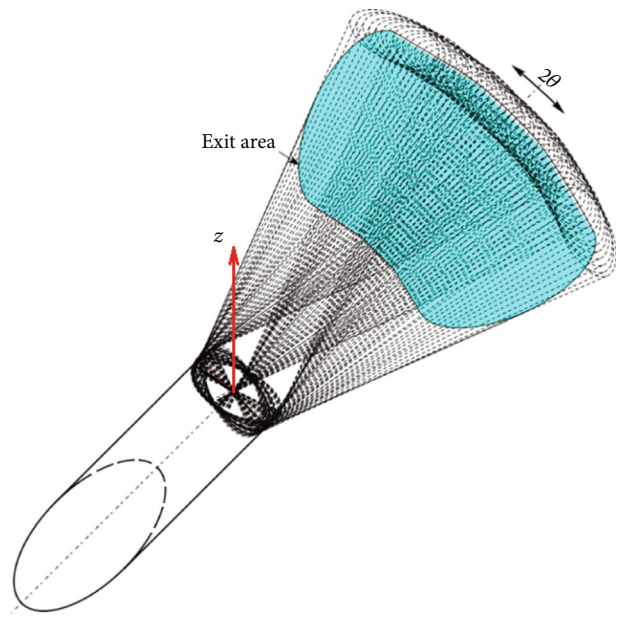

Figure 1: 3d visualization of the proposed diffusion hole.

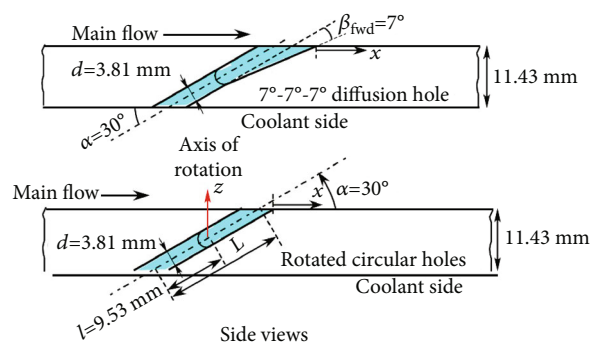

Figure 2: Test plate cross-section with film holes side views.

LED light (Thorlabs, M405L3 Mounted LED) and a CCD camera of 1600 by 1200-pixel resolution (ImageSource, DMK 23U274) with 610 nm light filter were installed above the test plate for data collection.

Test plates were made of 17.78 cm by 7.62 cm rectangular clear acrylic plastic of 1.143 cm thickness. Three equally spaced parallel film holes were drilled at a pitch to diameter ratio of $p/d = 6$ for each case. The machined test piece out of clear acrylic plastic, for $\theta = 21^\circ$, before the pressure-sensitive paint was applied is shown in Figure 6. The baseline geometry, the commonly used 7°-7°-7° diffusion hole, with which all new proposed film hole geometries were compared is shown in the top section of Figures 2 and 3. All film holes made an angle of $\alpha = 30^\circ$ with the main flow direction (inclination angle), and they all had a circular inlet section of $\ell = 2.5d$ long (Figure 2).

3. Pressure-Sensitive Paint and Calibration

Navarra [30] presented the pressure-sensitive paint (PSP) technique for the measurement of film cooling effectiveness.

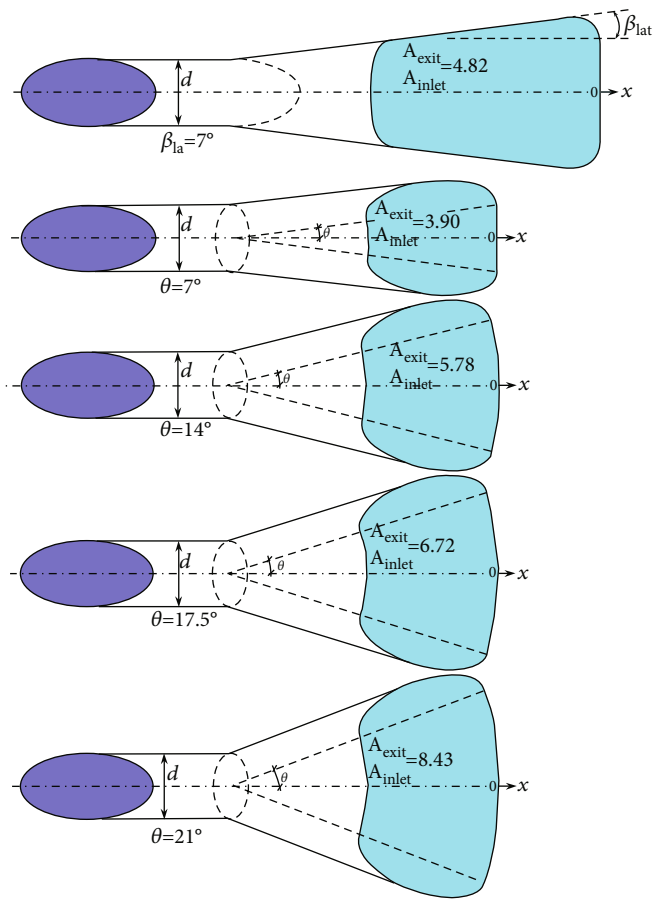

Figure 3: Film holes top views.

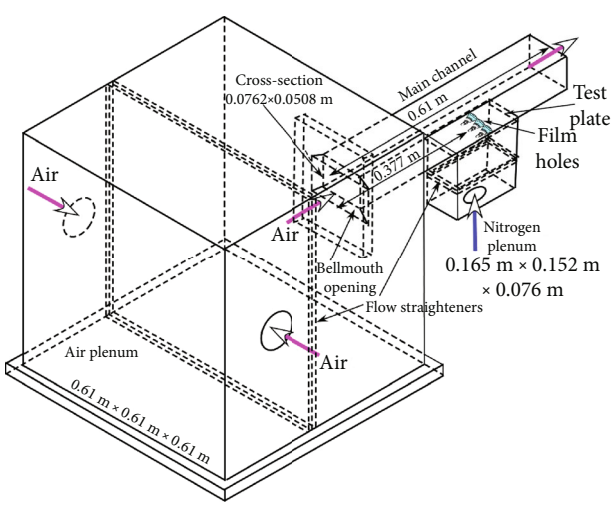

Figure 4: Schematics of the test rig.

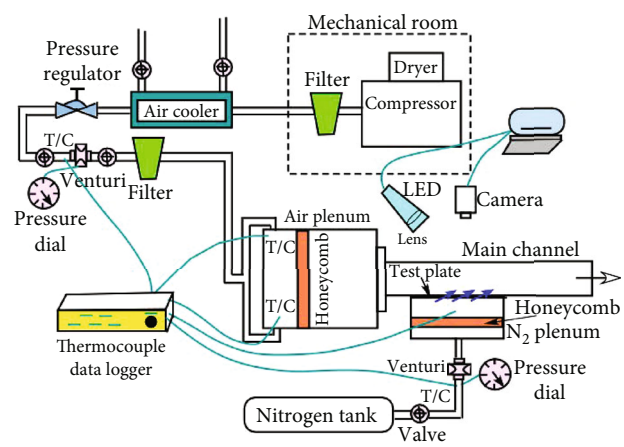

Figure 5: Test rig, associated accessories, and data collection equipment.

Remarkable improvement was achieved over the Temperature-Sensitive Paint (TSP) and Infrared (IR) techniques. The PSP technique is conducted under isothermal conditions; thus, there are little to no heat losses during the tests. This is a great advantage compared to the conventional methods in which one must account for any possible heat losses when data are reduced. Therefore, there is one less uncertainty in the extracted data. Additionally, earlier film effectiveness measurement techniques called for multiple thermocouples due to their ease of installation. However, the limited number of thermocouples at discrete points on the target areas could not produce a continuous thermal image of the surface accurately. This shortcoming, compounded by the number of leads and thermal losses

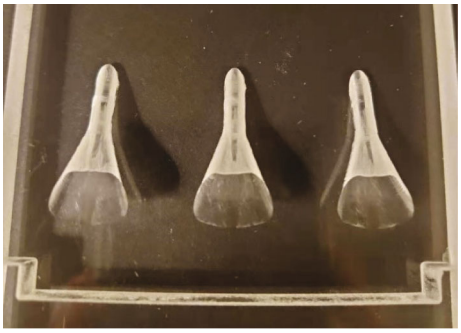

Figure 6: Machined test piece of $\theta = 21^\circ$ before testing.

associated with them increased the overall experimental uncertainty. In contrast, the PSP method generates a continuous image of the film cooling effectiveness (illuminance intensity) with high resolution over the entire surface under investigation. The UniFIB® pressure-sensitive paint from ISSI Innovative Solutions Inc was used in this study. This paint is a single component PSP optimized for a maximum luminescent signal while maintaining high pressure sensitivity and low temperature sensitivity. FIB Basecoat™ was used as the base coat before applying the PSP. This compound is sensitive to the oxygen partial pressure in the air-coolant mixture. When a UV light source (a 400 nm ultraviolet LED through a convex lens with 15 cm focal length, in this study) is cast on the painted surface, the paint illuminates with varying intensity depending on the partial pressure of the surrounding oxygen. This PSP property is exploited to our advantage to measure the film cooling effectiveness. Analogy between the mass and energy transport equations under identical boundary conditions (impermeable wall versus adiabatic wall) reveals that the film cooling effectiveness can be recast into

$$\eta = \frac{C_{aw} - C_\infty}{C_c - C_\infty} = 1 - \frac{1}{1 + \left(P_{O_2,\mathrm{air}}/P_{O_2,\mathrm{mix}} - 1\right) M_{N_2}/M_{\mathrm{air}}}. \quad (1)$$

The intensity ratio which is a function of the oxygen partial pressure can be modelled as

$$\mathrm{IR} = \frac{I_{\mathrm{ref}} - I_{\mathrm{black}}}{I - I_{\mathrm{black}}} = f\left(\frac{P}{P_{\mathrm{ref}}}\right) = f\left(P_{O_2}\right). \quad (2)$$

Before the start of the film effectiveness tests, the PSP was calibrated to determine a functional relationship between the luminescence and the oxygen partial pressure. A small test coupon sprayed with the same paint was placed in a sealed chamber connected to a vacuum pump. The chamber pressure was reduced from the atmospheric pressure (101.3 kPa) to about 3 kPa while a precision vacuum gauge (Pirani gauge, 275 series, by Kurt J. Lesker Company) measured the pressure inside the chamber, and five thermocouples at different locations measured the temperature. During the calibration process, the same lighting and camera arrangements as in the film effectiveness tests were used to excite and record the light intensity. The test coupon was

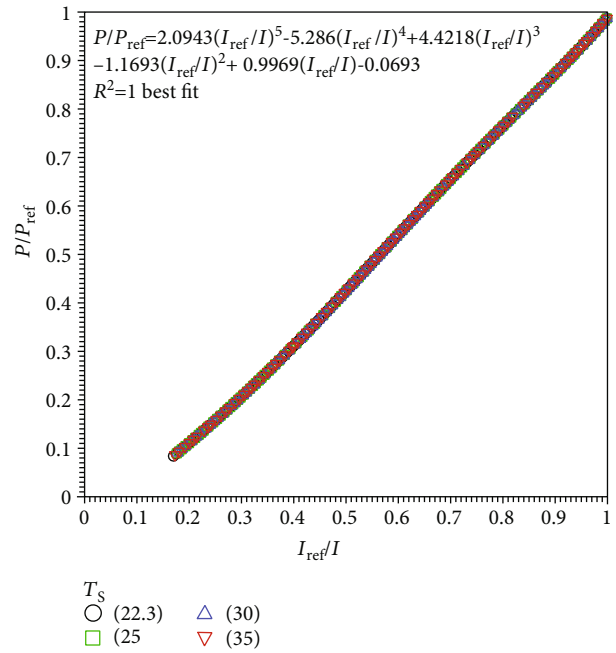

Figure 7: Calibration curve at different temperatures: 22.3, 25, 30, and 35°C.

calibrated for different surface temperatures of 22.3, 25, 30, and 35°C. Details of the calibration setup are given in Baldino and Taslim [14]. Figure 7 shows the calibration results indicating that the functional dependence of luminescence with the oxygen partial pressure remained the same in that range of surface temperature. The 5th-degree polynomial representing the best fit to the data was used throughout this study to determine film effectiveness.

4. Film Effectiveness Tests

A typical test started with setting the targeted main flow (air) without any coolant flow. Proper lighting was then set on the target surface, and the camera was focused. Once the system reached equilibrium, a baseline photo was captured to serve as the reference light intensity to which all captured photos during a film cooling effectiveness test were compared. Next, the coolant (nitrogen) was turned on and was set to a predetermined mass flow rate corresponding to the desired blowing ratio. Two critical-flow Venturis (choked at all conditions) measured the main and cooling flow mass flow rates. These mass flow rates, divided by the main channel and the film hole inlet cross-sectional areas, respectively, gave the $(\rho U)_{\mathrm{air}}$, $(\rho U)_{N_2}$ and the blowing ratio:

$$M = \frac{(\rho U)_{N_2}}{(\rho U)_{\mathrm{air}}} = \frac{\dot{m}_{N_2}/\pi/4d^2}{\dot{m}_{\mathrm{air}}/A_{\mathrm{passage}}}. \quad (3)$$

The freestream turbulence intensity in the main channel was measured to be 3.86%.

The vacuum pressure measurement sensor was found to be the main source of uncertainty. Since each test takes only

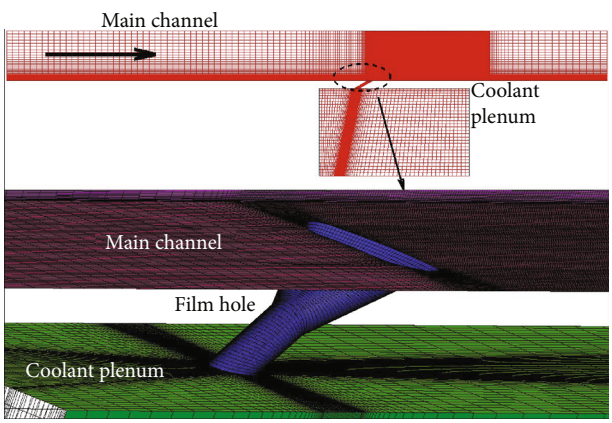

Figure 8: Computational model and mesh distribution around a typical film hole.

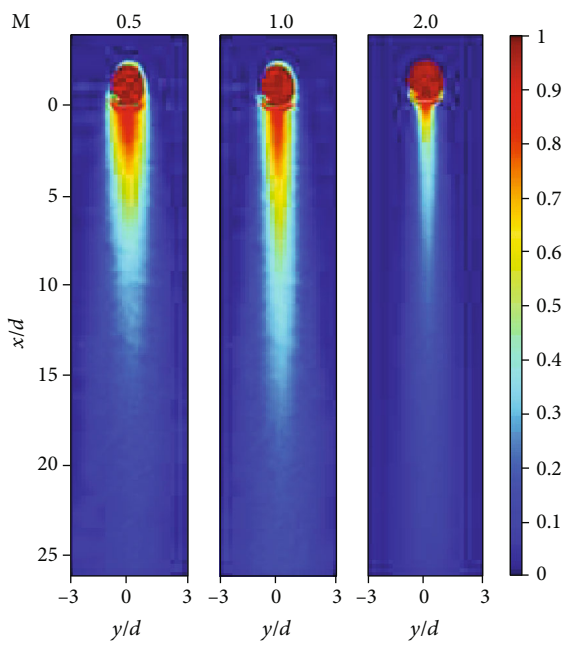

Figure 9: Experimental contours of $\theta = 7°$.

a few minutes, the decay of PSP becomes insignificant [31]. Errors associated with the LED lighting and CCD camera as well as the slight temperature variations (Figure 7) are insignificant. Therefore, the film cooling effectiveness uncertainty, following the method of Kline [32], can be expressed as

$$\delta\eta = \sqrt{\left(\frac{\partial\eta}{\partial P_{O_2}}\right)^2 \delta P_{O_2}^2}. \quad (4)$$

The derivative of the film effectiveness with respect to the oxygen partial pressure from Equation (1) is

$$\frac{\delta\eta}{\delta P_{O_2}} = -\frac{M_{N_2}/M_{air}21.21}{\left(M_{N_2}/M_{air}21.21/P_{O_2} + 1 - M_{N_2}/M_{air}\right)^2 P_{O_2}}, \quad (5)$$

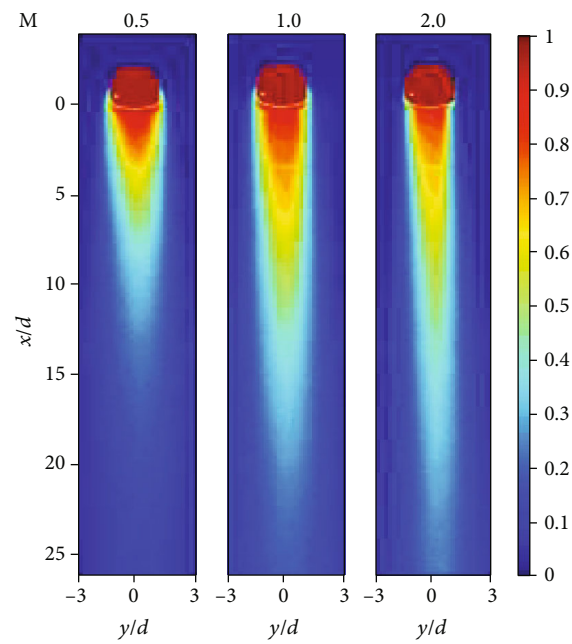

Figure 10: Experimental contours of $\theta = 14°$.

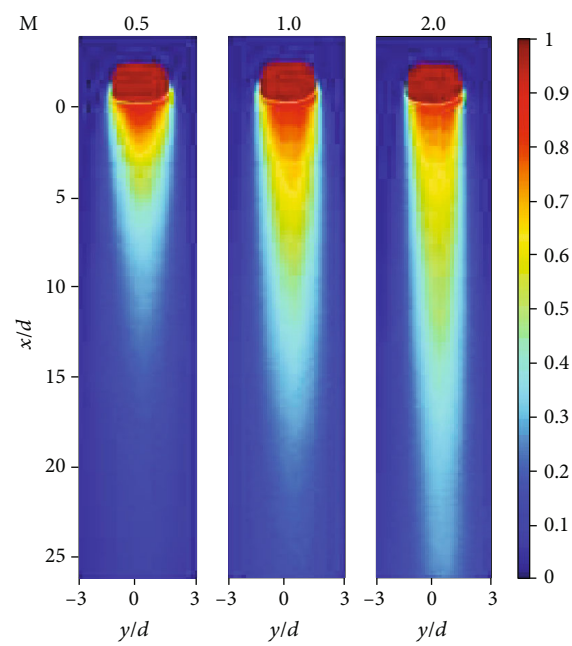

Figure 11: Experimental contours of $\theta = 17.5°$.

where 21.21 is the mole fraction of oxygen in air. The vacuum pressure sensor accuracy δP depends on the measured pressure:

$$\begin{cases} \text{if } P < 50\text{kPa} \longrightarrow \delta P = \pm 10\% \text{of reading}, \\ \text{if } P > 50\text{kPa} \longrightarrow \delta P = \pm 2.5\% \text{of reading}. \end{cases} \quad (6)$$

Therefore, the uncertainty of the oxygen partial pressure (δP_{O_2}) is given by the uncertainty of the absolute

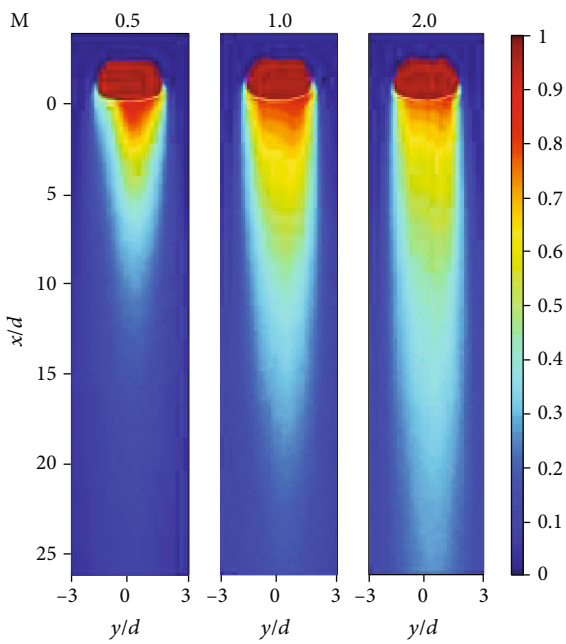

Figure 12: Experimental contours of $\theta = 21^\circ$.

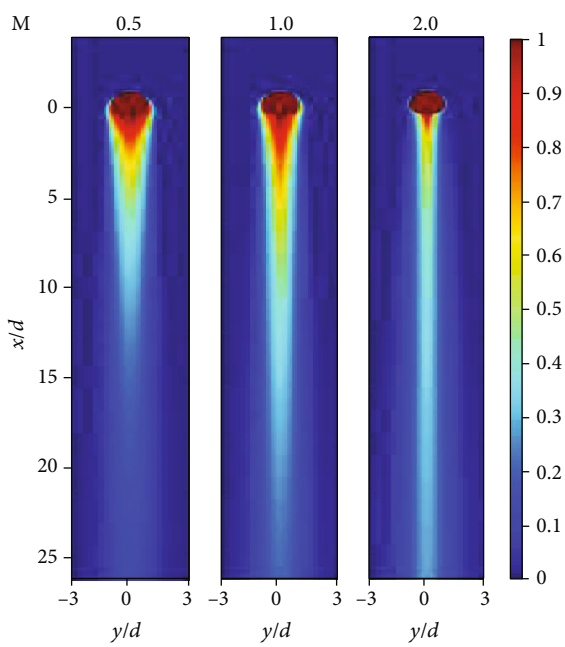

Figure 13: CFD contours of $\theta = 7^\circ$.

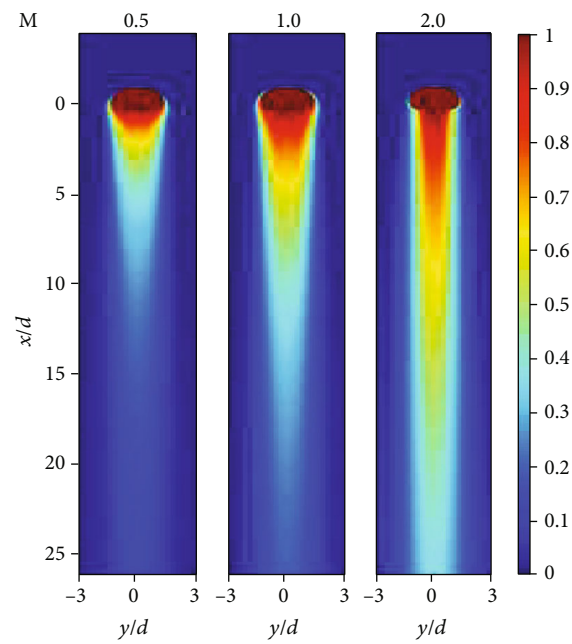

Figure 14: CFD contours of $\theta = 14^\circ$.

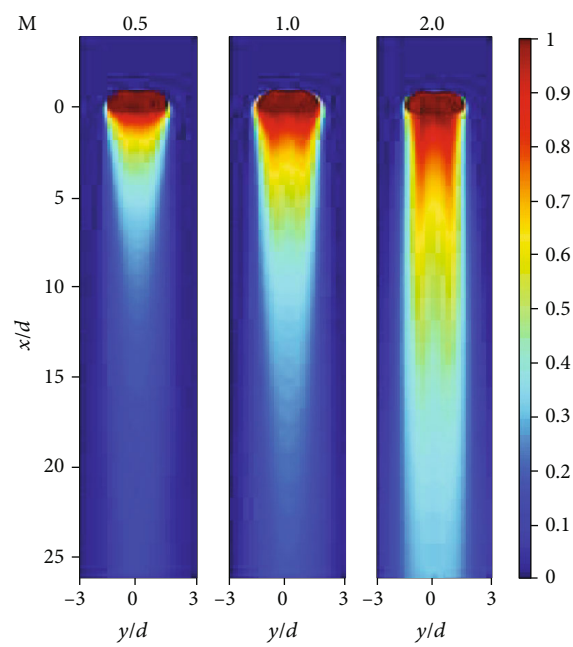

Figure 15: CFD contours of $\theta = 17.5^\circ$.

pressure times the oxygen concentration percentage within the air:

$$\begin{cases} \delta P_{O_2} = 0.21\delta P = 0.10 P_{O_2}, & \text{if } P < 50\text{kPa}, \\ \delta P_{O_2} = 0.21\delta P = 0.025 P_{O_2}, & \text{if } P > 50\text{kPa}. \end{cases} \quad (7)$$

In conclusion, the maximum effectiveness uncertainty was calculated to be about ±5%. More details of the uncertainty analysis are discussed in Baldino and Taslim [14].

5. Computational Model

The computational domain included the main channel, the coolant plenum, and the five film hole geometries. The solid models were created in Solidworks and were imported to the powerful ICEM-CFD™ mesher by Ansys. Figure 8 shows the computational domain and details of the mesh distribution around a typical middle hole geometry with two symmetric side walls. Cells in all models were entirely hexahedral, a preferred choice for CFD analyses, and were varied in size

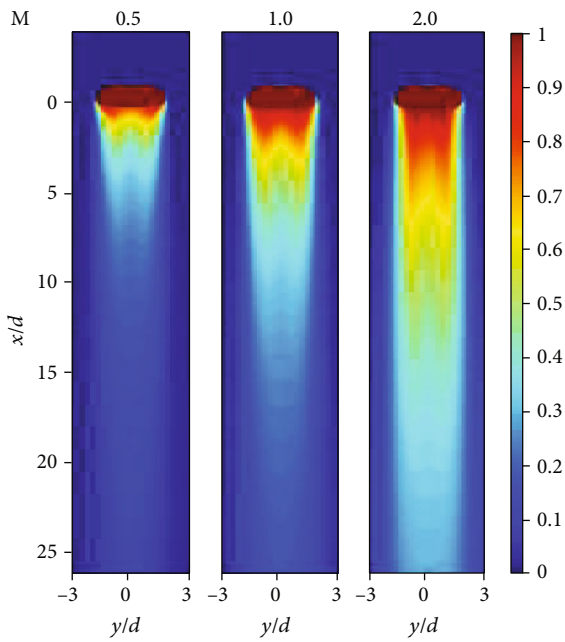

Figure 16: CFD contours of $\theta = 21^\circ$.

bigeometrically from the boundaries to the center of the computational domain in order to have finer mesh close to the boundaries. The CFD analyses were performed using Fluent/UNS solver by Ansys, Inc., a pressure correction-based, multiblock, multigrid, unstructured/adaptive solver. Coolant and main channel air mass flow rates for the numerical models were identical to those of the experiments. They were at 300 K and 320 K, respectively. The main channel exit had a pressure boundary condition identical to that of the lab. The realizable k-ε turbulence model was employed in combination with the enhanced wall function. Other turbulence models such as k-ω and standard k-ε turbulence model were tried but did not reduce the difference with the experimental data. To study the details at the wall region, the average $y+$ for the first layer of cells was controlled to be below 5 for all cases. The turbulence intensity of the main flow was set to be identical to that of the tests. The main flow boundary layer thickness was calculated to be around $5d$ so that the coolant was not disturbing its development. Mesh independence was achieved at about 3 million hexahedral elements for a typical model.

All models, however, were run with a total number of hexahedral elements of about 4 million. Residual sums for all variables in all models were less than 1×10^{-7}. Convergence, for most cases, was achieved at around 30,000 iterations.

6. Results and Discussion

Experimental film cooling effectiveness contours downstream of the four new geometries are shown in Figures 9–12. Each figure represents three blowing ratios of $M = 0.5$, 1, and 2. The slight asymmetry in some contours is due to machining imperfections. Visual comparison of these contours shows that the case of $\theta = 21^\circ$ does a much more effective coverage of the target surface, and, in particular, for the larger blowing ratio of 2, the coolant extends farther, both axially and laterally. Apart from the $\theta = 7^\circ$ case, the area covered by the coolant increases as the blowing ratio increases from 0.5 to 2. In $\theta = 7^\circ$ geometry, its small exit area creates a strong jet which results in a blow-off, especially for $M = 2$. However, as θ increases, the larger hole exit area leads to the diffusion of coolant in the lateral direction that weakens the kidney vortices and consequently increases the film coverage. Similarly, the CFD contours of film cooling

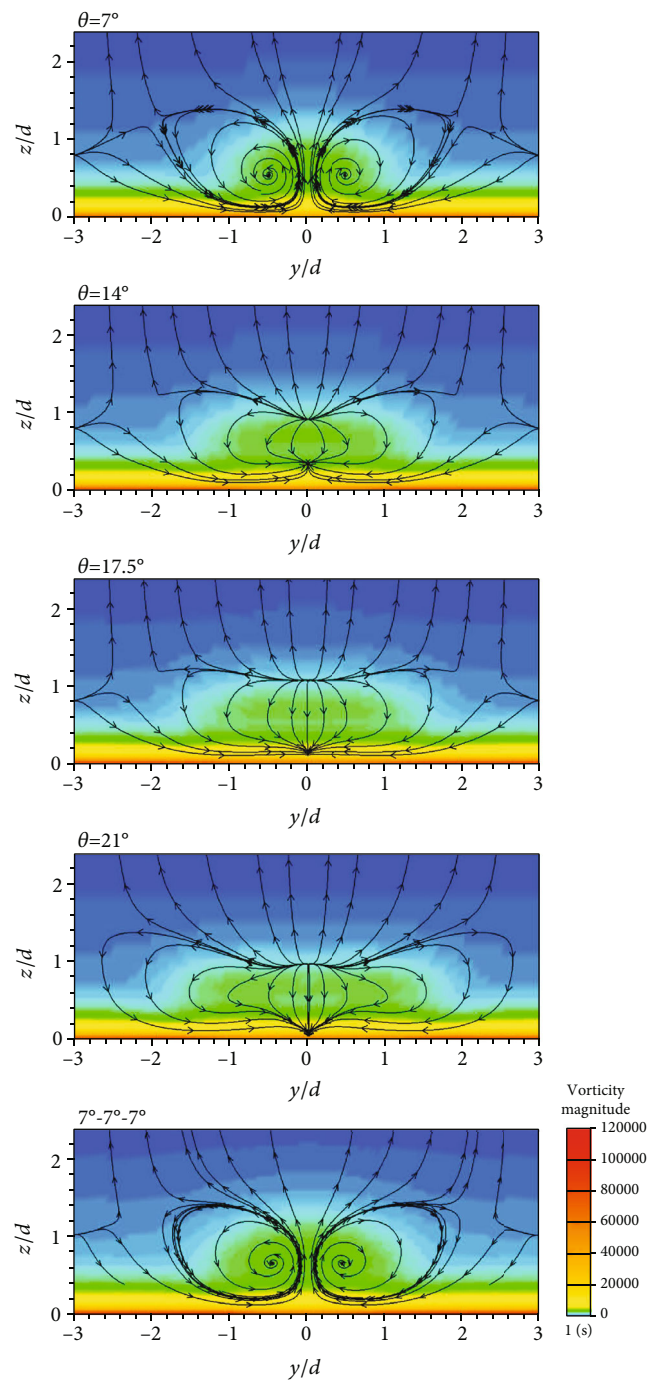

Figure 17: CFD vorticity magnitude contours for $M = 0.5$ at $x/d = 5$.

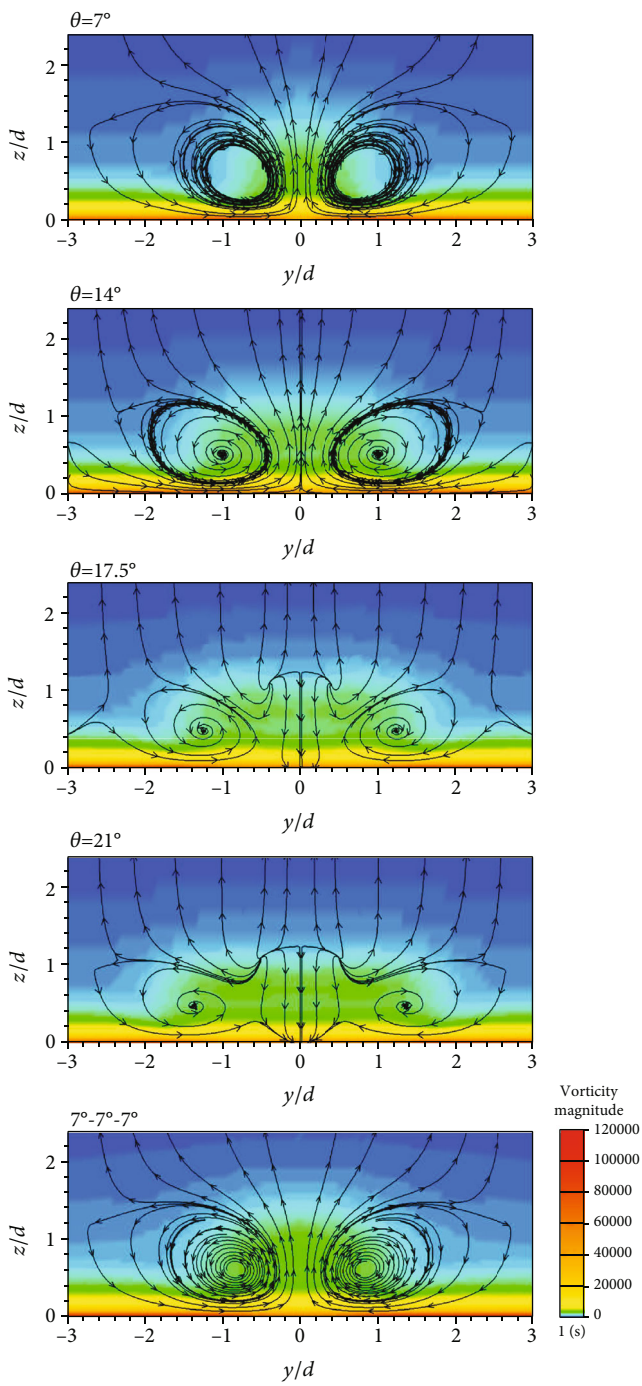

Figure 18: CFD vorticity magnitude contours for $M = 1$ at $x/d = 5$.

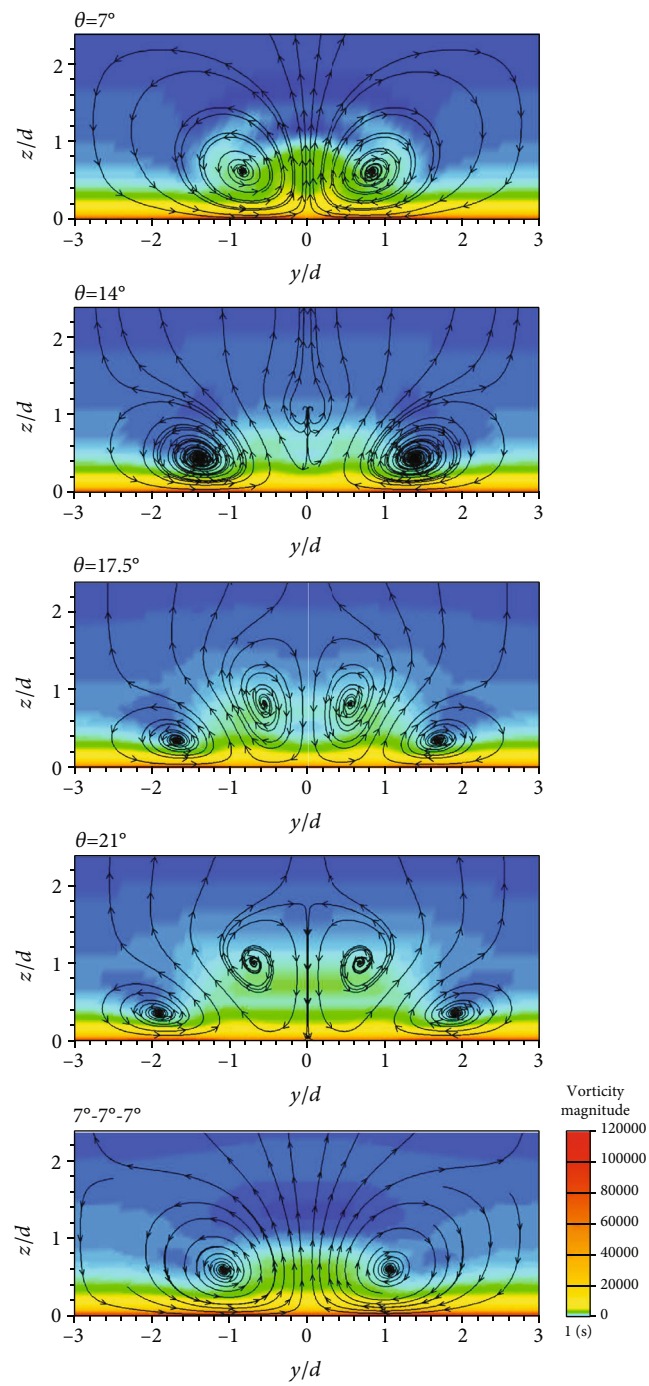

Figure 19: CFD vorticity magnitude contours for $M = 2$ at $x/d = 5$.

effectiveness downstream of these four geometries are shown in Figures 13–16. These contours are in good agreement with those of the experimental results as $\theta = 21^\circ$ represents the best coverage, and the film cooling effectiveness increases with the blowing ratio. The double streaks in Figures 15 and 16 could be an indication of vortex generation due to higher diffusion of the film hole at the exit, compounded by the sharp edges modelled in the CFD runs. Figures 17–19, to be discussed shortly, show the migration of the main hot flow to the centerline for these cases thus reducing the film effectiveness along the centerline. The experimental geometry, however, had a slight rounding on the exit edge, dictated by the milling machine tolerances that prevented the formation of exit vortices.

The area-averaged effectiveness values between $y/d = (-3, 3)$ in Figures 9–16 are shown in Tables 1 and 2. The experimental film effectiveness results are slightly higher than those of the CFD analyses for $M = 0.5$ and 1.0. At $M = 2$, however, the experimental results fell below the CFD results. Other conventional turbulence models such as standard k-ε

Table 1: Area-averaged film effectiveness from $x/d = 0$ to 25.

	M	$\theta = 7^\circ$	$\theta = 14^\circ$	$\theta = 17.5^\circ$	$\theta = 21^\circ$	7° -7°-7°
Test	0.5	0.1603	0.1936	0.1888	0.1830	0.1844
	1.0	0.1656	0.2538	0.2626	0.2734	0.2369
	2.0	0.0893	0.2257	0.2654	0.3015	0.1973
CFD	0.5	0.1296	0.1499	0.1562	0.1600	0.1127
	1.0	0.1703	0.2377	0.2583	0.2674	0.1585
	2.0	0.1181	0.2867	0.3221	0.3417	0.1794

Table 2: CFD area-averaged film effectiveness from $x/d = 0$ to 40.

	M	$\theta = 7^\circ$	$\theta = 14^\circ$	$\theta = 17.5^\circ$	$\theta = 21^\circ$	7°-7°-7°
CFD	0.5	0.1083	0.1237	0.1277	0.1250	0.1103
	1.0	0.1328	0.1877	0.2046	0.2090	0.1636
	2.0	0.1141	0.2474	0.2944	0.3073	0.1853

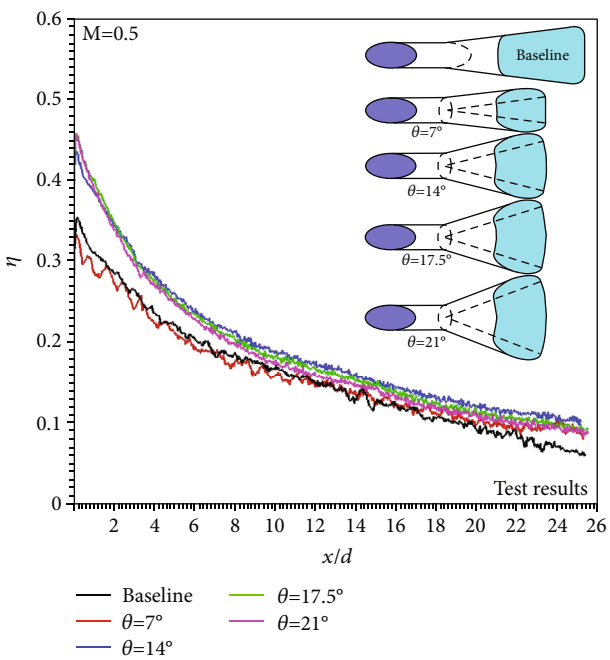

Figure 20: Streamwise variation of measured film effectiveness (spanwise-averaged at each point) for the blowing ratio of 0.5.

and k-ω with SST options were turned on in our CFD runs with no significant improvement in the final results. Both experimental and CFD results show that the case of $\theta = 21^\circ$ has the best performance with all blowing ratios. This behaviour is expected as the same amount of coolant emerges from an area with about 1.75 times the baseline hole exit area at an average velocity of about 57% of that in the baseline hole case with less interactions with the main flow. Therefore, it presents a more effective coverage of the target area. The spanwise-averaged film effectiveness variations of experimental as well as numerical results in the flow direction are shown in Figures 20–25. The solid lines represent the test data while the broken lines show the numerical results. It should be noted that $x/d = 0$ corresponding to

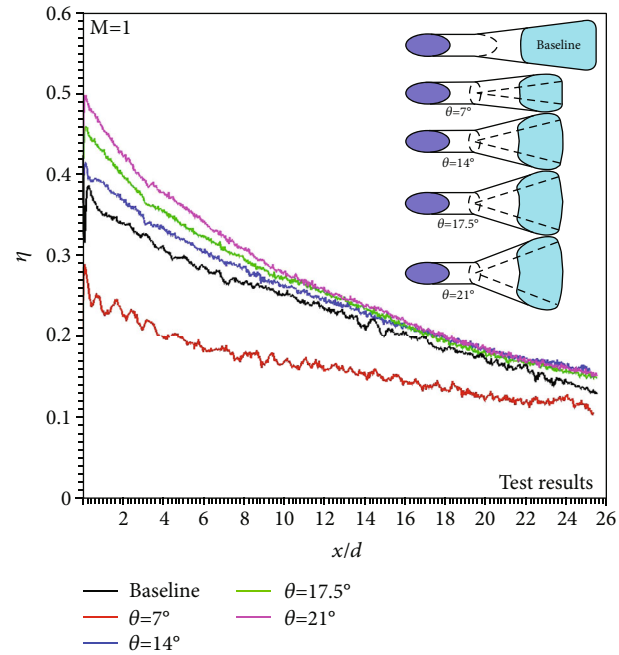

Figure 21: Streamwise variation of measured film effectiveness (spanwise-averaged at each point) for the blowing ratio of 1.

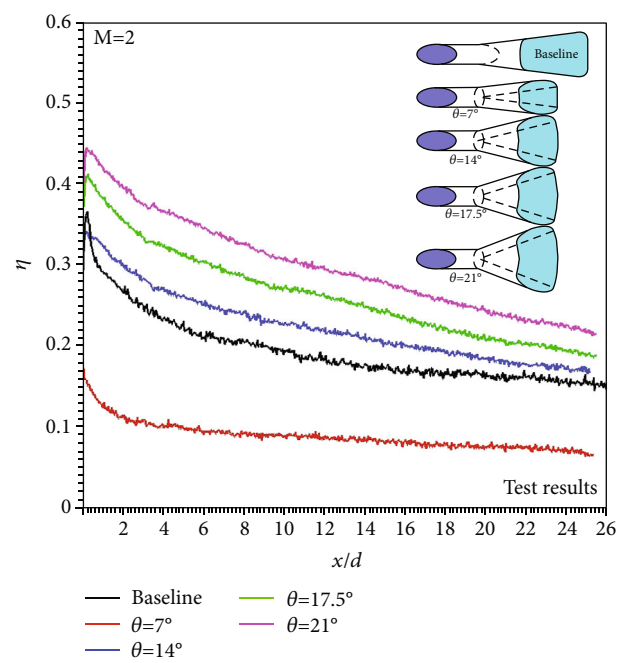

Figure 22: Streamwise variation of measured film effectiveness (spanwise-averaged at each point) for the blowing ratio of 2.

the farthest exit, especially at higher blowing ratios, are expected. We included this geometry to see the threshold beyond which the proposed geometry performs better than the diffusion holes. The agreement between the test data and numerical results is fair and improves with the blowing ratio. It should be noted that $x/d = 0$ corresponds to the farthest exit point of the cooling hole on the target surface for

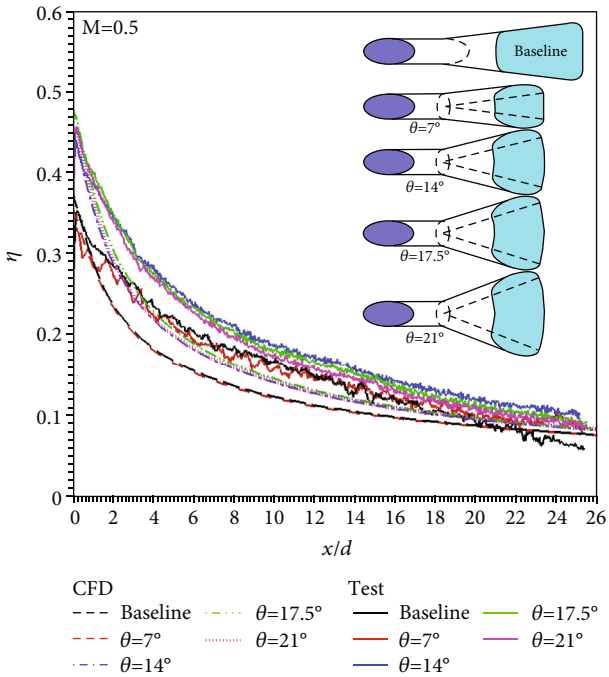

Figure 23: Streamwise variation of test and CFD film effectiveness (spanwise-averaged at each point) for the blowing ratio of 0.5.

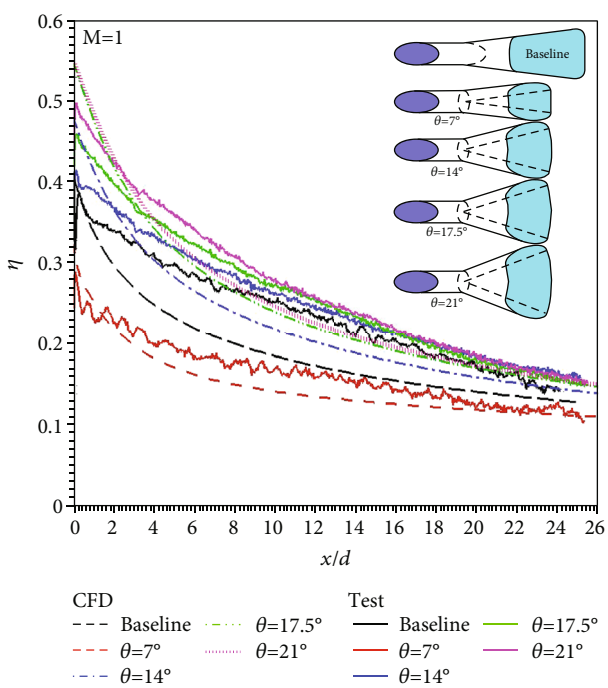

Figure 24: Streamwise variation of test and CFD film effectiveness (spanwise-averaged at each point) for the blowing ratio of 1.

each geometry as is shown in Figure 3. The results are compared with the result of 7°-7°-7° diffusion hole, our baseline geometry. Several observations are made: For the blowing ratios of 1 and 2, the new proposed file hole geometries with $\theta = 14^\circ$, 17.5°, and 21° perform much better than the 7°-7°-7° diffusion hole.

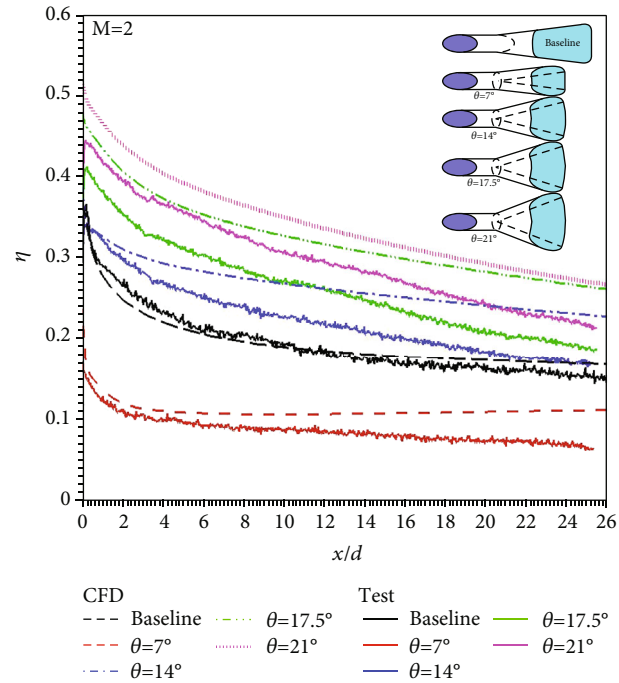

Figure 25: Streamwise variation of test and CFD film effectiveness (spanwise-averaged at each point) for the blowing ratio of 2.

The inferior performance of $\theta = 7^\circ$ compared with the performance of the diffusion baseline hole is understandable as the $\theta = 7^\circ$ hole is very close to a straight-through cylindrical hole and the occurrence of jet lift-off and presence of kidney vortices.

Figure 26 represents a visual comparison of the film effectiveness performance for the five film hole geometries. With the same scales in all graphs, it can be seen that, as the rotation angle θ increases, the film effectiveness in the stream-wise direction increases. It also shows that $\theta = 17.5^\circ$ and 21° geometries present superior film coverage, compared to the conventional 7°-7°-7° diffusion hole.

Figures 17–19 show the CFD vorticity magnitude contours along with the streamlines for all cases at all blowing ratios. These contours are generated on a plane normal to the target surface at $x/d = 5$. The baseline geometry, on the bottom section of these figures, and the $\theta = 7^\circ$ geometry, on the top section of these figures, are affected by the formation of kidney vortices that push the coolant away from the target surface, evidenced by the velocity direction on the streamlines. These two geometries, as we noticed in the previous sections, produced lower film effectiveness values. Figure 27 shows the bird's eye view of the vorticity magnitude contours and velocity vectors on a plane at a distance of $0.05d$ from the target surface. The strong main flow and coolant interactions, represented by the large intersecting vectors, create kidney vortices that adversely affect the film coverage. Examples of those cases are the first and second cases in the third column. Table 3 gives a general performance evaluation of these five geometries based on the vorticity contour observations. The top and bottom rows correspond to these two geometries. As θ increases, we see

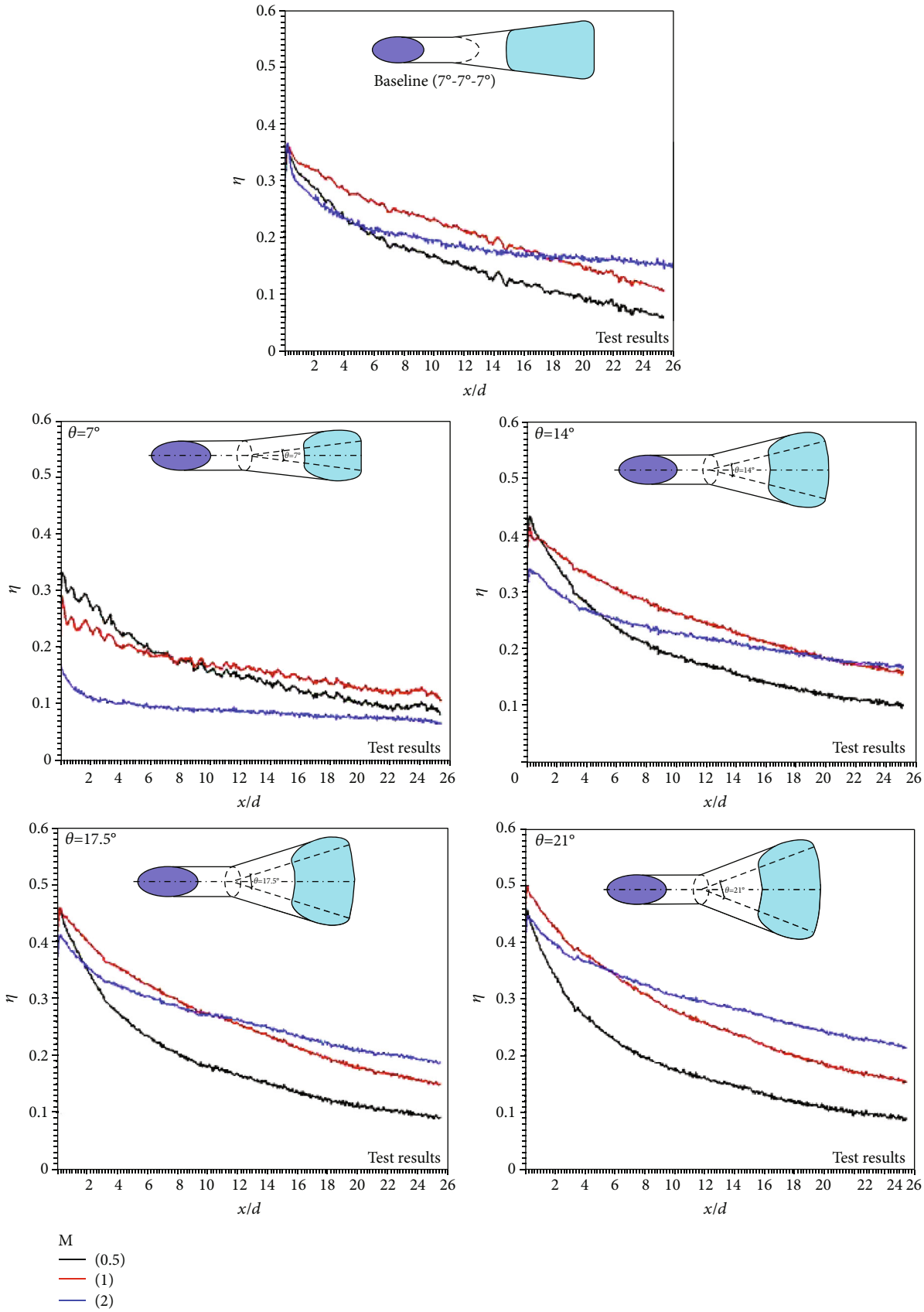

Figure 26: A comparison between the measured film effectiveness performance of the five film hole geometries.

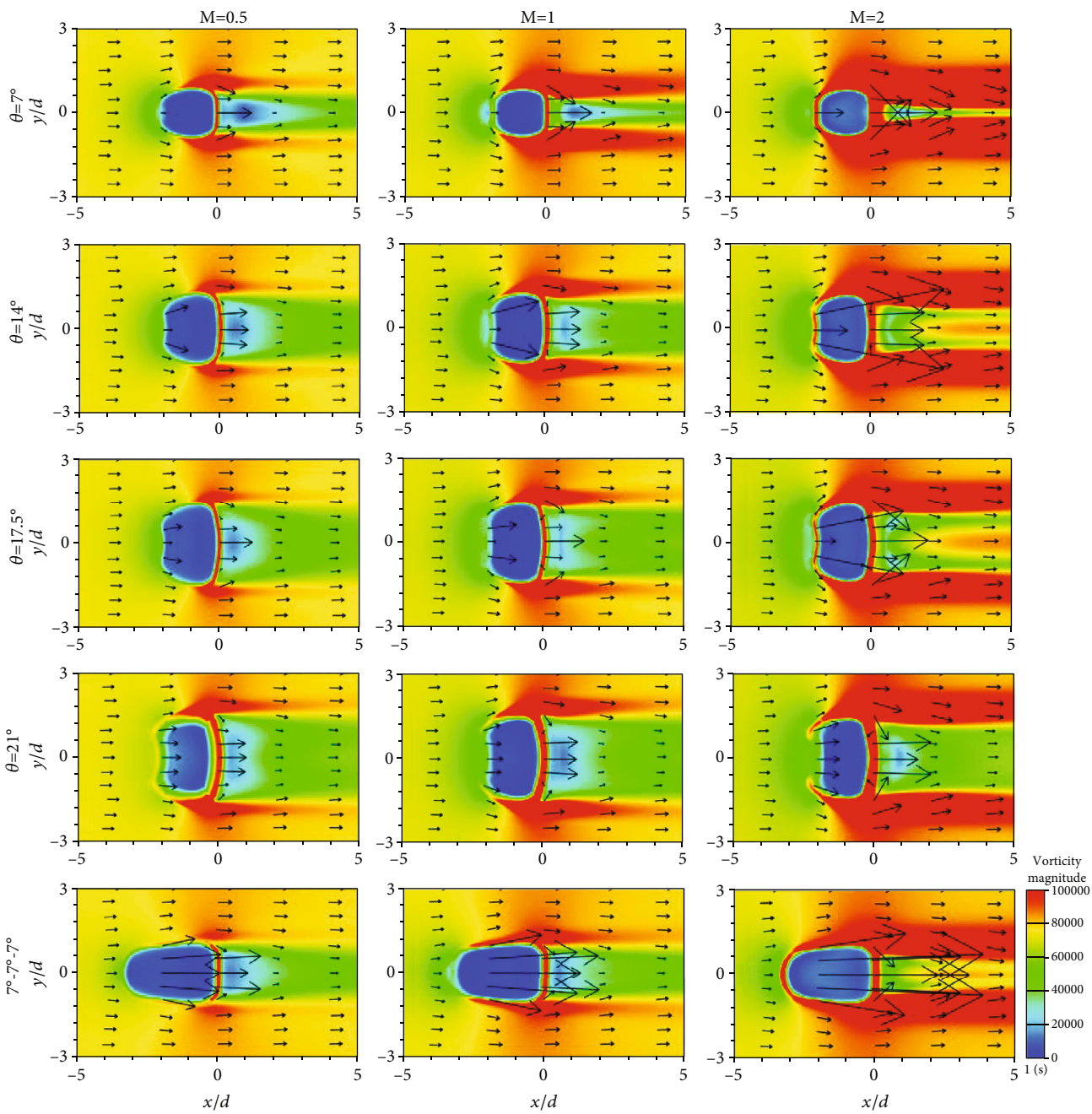

Figure 27: CFD vorticity magnitude contours and velocity vectors at $z/d = 0.05$ (looking down on the target plate).

Table 3: Antivortex performance of different geometries.

Geometry	$M = 0.5$	$M = 1.0$	$M = 2.0$
$\theta = 7^\circ$	No antivortex action	No antivortex action	No antivortex action
$\theta = 14^\circ$	Good antivortex action	No antivortex action	No antivortex action
$\theta = 17.5^\circ$	Good antivortex action	Good antivortex action	Strong antivortex action
$\theta = 21^\circ$	Good antivortex action	Good antivortex action	Strong antivortex action
7°-7°-7° baseline	No antivortex action	No antivortex action	No antivortex action

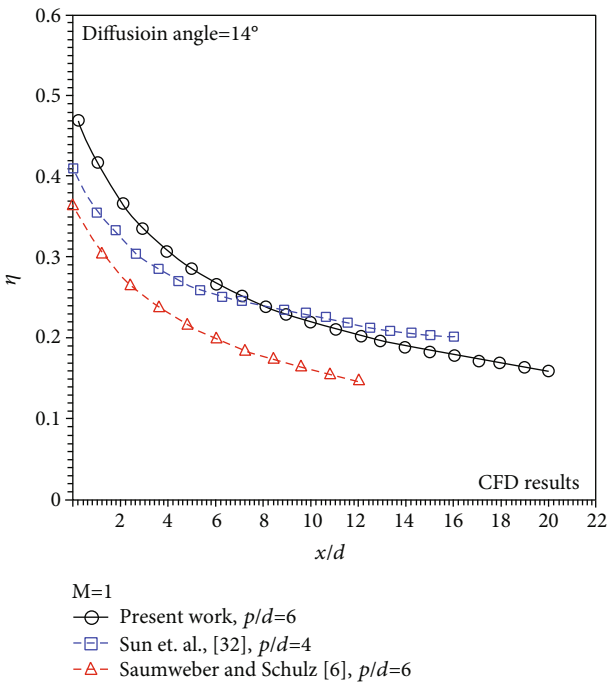

Figure 28: A comparison between the present work and CFD studies in open literature.

a different flow structure. The remaining three new geometries ($\theta = 14^\circ$, 17.5°, and 21°) create strong antivortex flow structures for the blowing ratio of 0.5 (Figures 17, 18 and 26) resulting in downward coolant velocity vectors towards the target surface. Geometries corresponding to the higher range of θ perform well as antivortex geometries.

Figure 28 shows the film effectiveness comparison between the present study and those in open literature [6, 33]. For the 14° lateral expansion angle, the present shape outperforms the other two geometries at the hole exit zone. The geometry of Sun et al. [33] shows higher effectiveness at $x/d > 10$ due to its small pitch to diameter ratio compared to the present study ($p/d = 6$). In general, the current curved diffusion design increased the overall film cooling effectiveness.

As for further increasing the rotation angle θ beyond 21° for possible further improvements in film cooling effectiveness, for a commonly practiced hole pitch to diameter ratio, p/d, of 6, any further increase in the rotation angle would bring the adjacent hole exits too close to each other, thus compromising the structural integrity as well as the film cooling effectiveness due to the interactions of the coolant ejecting from the adjacent hole exits.

7. Conclusion

Experimental and numerical studies were conducted in this investigation on four new film hole geometries. Pressure-sensitive paint was used to measure the film effectiveness at blowing ratios of 0.5, 1.0, and 2.0. Comparisons were made between the film effectiveness results of these proposed new film holes and those of the conventional 7°-7°-7° diffusion hole. Major conclusions of this investigation are the following: (a) as the hole rotation angle, θ, increases, the film effectiveness downstream the hole exit increases; (b) the best film effectiveness performance was presented by the hole with $\theta = 21^\circ$; (c) the smallest rotation angle, $\theta = 7^\circ$, exhibited the worst performance due to its smallest exit area that resulted in coolant lift-off; (d) for all tested blowing ratios, the cases of $\theta = 14^\circ$, 17.5°, and 21° showed superior film effectiveness performance, compared with the conventional 7°-7°-7° diffusion hole; and (e) the numerical results are in good agreement with the experimental data.

Nomenclature

$A_{passage}$: Main flow passage area (38.71 cm^2)
C: Chemical concentration (%)
d: Film hole inlet diameter (Figure 3) (3.81 mm)
D_h: Main passage hydraulic diameter (60.96 mm)
I: Light intensity (pixel intensity value)
IR: The ratio of reference light intensity and measured intensity
L: Total axial length of each film hole (Figure 2)
ℓ: Feed (entrance) hole length (Figure 2, 9.53 mm)
$\dot{m}_{N_2}$: Nitrogen flow rate in each tripod (kg/s)
$\dot{m}_{air}$: Main channel air mass flow rate (kg/s)
M: Blowing ratio $(\dot{m}_{N_2}/\pi d^2/4)/(\dot{m}_{air}/A_{passage})$
M_c: Coolant molecular weight (28 kg/kmol)
M_∞: Mainstream (air) molecular weight (28.97 kg/kmol)
p: Hole pitch (22.86 mm)
P: Pressure (Pa)
PSP: Pressure-sensitive paint
$P_{O_2,air}$: Oxygen partial pressure in main channel approach air (Equation (1), 21 kPa)
$P_{O_2,mix}$: Oxygen partial pressure at a given point downstream the film holes (Equation (1), kPa)
Re: Reynolds number based on the passage hydraulic diameter $((\rho U D_h/\mu) = 87200)$
T: Temperature
T^*: Dimensionless temperature
TSP: Temperature-sensitive paint
U: Main passage air velocity (m/s)
β_{fwd}: Shaped hole forward angle (Figure 2)
β_{lat}: Shaped hole lateral angle (Figure 3)
η: Film cooling effectiveness
μ: Air dynamic viscosity (kg/(m·s))
θ: Hole rotation angle (Figures 1 and 3)
ρ: Air density (kg/m^3).

Subscripts

aw: Adiabatic wall
blk: Black
c: Coolant
O_2: Diatomic oxygen
N_2: Nitrogen
ref: Reference
∞: Channel mainstream.

Data Availability

Data files are available upon request.

Conflicts of Interest

The authors declare that they have no conflicts of interest.

References

[1] S. S. Papell, *Effect on gaseous film cooling of coolant injection through angled slots and normal holes*, National Aeronautics and Space Administration, 1960, NASA-TN-D-299.

[2] J. P. Hartnett, R. C. Birkebak, and E. R. G. Eckert, "Velocity distributions, temperature distributions, effectiveness, and heat transfer for air injected through a tangential slot into a turbulent boundary layer," *Journal of Heat Transfer*, vol. 83, no. 3, pp. 293–305, 1961.

[3] R. J. Goldstein, "Film cooling," in *Advances in Heat Transfer*, vol. 7, pp. 321–379, Academic Press, San Diego, 1971.

[4] G. Barigozzi, G. Benzoni, G. Franchini, and A. Perdichizzi, "Fan-shaped hole effects on the aero-thermal performance of a film-cooled endwall," *Journal of Turbomachinery*, vol. 128, no. 1, pp. 43–52, 2006.

[5] A. Kohli and D. G. Bogard, "Effects of hole shape on film cooling with large angle injection," ASME International Gas Turbine and Aeroengine Congress, 1999, 99-GT-165.

[6] C. Saumweber and A. Schulz, "Effect of geometry variations on the cooling performance of fan-shaped cooling holes," *Journal of Turbomachinery*, vol. 134, no. 6, article 061008, 2012.

[7] Y. Lu, *Effect of hole configurations on film cooling from cylindrical inclined holes for the application to gas turbine blades*, Louisiana State University, 2007, Ph.D. Dissertation.

[8] C. LeBlanc, D. P. Narzary, and S. V. Ekkad, "Film-cooling performance of antivortex hole on a flat plate," *Journal of Turbomachinery*, vol. 135, no. 6, article 61009, 2013.

[9] Y. Yao, J. Zhang, and Y. Yang, "Numerical study on film cooling mechanism and characteristics of cylindrical holes with branched jet injections," *Propulsion and Power Research*, vol. 2, no. 1, pp. 30–37, 2013.

[10] R. P. Schroeder and K. A. Thole, "Adiabatic effectiveness measurements for a baseline shaped film cooling hole," 2014, *Paper* # GT2014-25992.

[11] S. Khajehhasani and B. A. Jubran, "Numerical assessment of the film cooling through novel sister shaped single hole schemes," *Numerical Heat Transfer, Part A: Applications*, vol. 67, no. 4, pp. 414–435, 2015.

[12] R. P. Schroeder and K. A. Thole, "Effect of in-hole roughness on film cooling from a shaped hole," *Journal of Turbomachinery*, vol. 139, no. 3, pp. 031004-1–031004-9, 2017.

[13] S. Balaji, F. Yang, and M. E. Taslim, "A comperative experimental study between the film effectiveness of trench and diffusion film holes," *International Journal of Thermal Sciences*, vol. 161, p. 106713, 2021.

[14] F. Baldino and M. E. Taslim, "Experimental film cooling effectiveness of multi-row patterns on flat and step-down surfaces," 2019, Paper # GT-2019-90108.

[15] R. S. Bunker, "A review of shaped-hole turbine film-cooling technology," *Journal of Turbomachinery*, vol. 127, no. 4, pp. 441–453, 2005.

[16] B. A. Haven, D. K. Yamagata, M. Kurosaka, S. Yamawaki, and T. Maya, "Anti-kidney pair of vortices in shaped holes and their influence on film cooling effectiveness," 1997, Paper # 97-GT-045.

[17] C. Han, J. Ren, and H. Jiang, "Multi-parameter influence on combined-hole film cooling system," *International Journal of Heat and Mass Transfer*, vol. 55, no. 15-16, pp. 4232–4240, 2012.

[18] K. Kusterer, A. Elyas, D. Bohn, T. Sugimoto, R. Tanaka, and M. Kazari, "Film cooling effectiveness comparison between shaped-and double jet film cooling holes in a row arrangement," 2010, Paper # GT2010-22604.

[19] Z. Wang, J. J. Liu, and C. Zhang, "Impacts of geometric parameters of double-jet film cooling on anti-kidney vortex structure and cooling effectiveness," 2013, Paper # GT2013-94038.

[20] S. Park, H. Chung, S. M. Choi, S. H. Kim, and H. H. Cho, "Design of sister hole arrangements to reduce kidney vortex for film cooling enhancement," *Journal of Mechanical Science and Technology*, vol. 31, no. 8, pp. 3981–3992, 2017.

[21] K. Kusterer, A. Elyas, D. Bohn, T. Sugimoto, and R. Tanaka, "Double-jet film-cooling for highly efficient film-cooling with low blowing ratios," 2008, Paper # GT2008-50073.

[22] F. Yang and M. E. Taslim, "Experimental film cooling effectiveness of three-hole-branch circular holes," *International Journal of Rotating Machinery*, vol. 2021, Article ID 6691128, 2021.

[23] J. Zhou, X. Wang, J. Li, and H. Lu, "Effects of diameter ratio and inclination angle on flow and heat transfer characteristics of sister holes film cooling," *International Communications in Heat and Mass Transfer*, vol. 110, article 104426, 2020.

[24] J. Yao, P. Su, J. He, J. Wu, J. Lei, and Y. Fang, "Experimental and numerical investigations on double-jet film-cooling with different mainstream incidence angles," *Applied Thermal Engineering*, vol. 166, article 114737, 2020.

[25] R. Zhu, E. Lin, T. Simon, and G. Xie, "Investigation and numerical simulation on film cooling performance with an anti-vortex hole design: influences of diameter ratio," *International Communications in Heat and Mass Transfer*, vol. 121, article 105118, 2021.

[26] L. Wang, X. Li, J. Ren, and H. Jiang, "The interaction between upstream and downstream film cooling rows in flow field and heat transfer," *International Journal of Thermal Sciences*, vol. 149, article 106176, 2020.

[27] R. S. Bunker and B. P. Lacy, "Articles which include chevron film cooling holes, and related processes," p. B2, 2010, US patent # 8,905,713.

[28] M. C. Morris, D. Waldman, M. F. Malak, and L. Tapia, "Gas turbine engine components with lateral and forward sweep film cooling holes," p. B2, 2012, US patent # 10,113,433.

[29] S. Dutta, G. M. Itzel, and B. P. Lacy, "Film hole trench," p. B2, 2011, US patent # 8,858,175.

[30] K. R. Navarra, *Development of the pressure-sensitive-paint technique for advanced turbomachinery applications*, Virginia Tech, 1997, Doctoral dissertation.

[31] B. Johnson and H. Hu, "Measurement uncertainty analysis in determining adiabatic film cooling effectiveness by using pressure sensitive paint technique," *Journal of Turbomachinery*, vol. 138, no. 12, article 121004, 2016.

[32] S. J. Kline, *Describing uncertainty in single sample experiments, Mechanical engineering*, vol. 75, pp. 3–8, 1953.

[33] X. Sun, G. Zhao, P. Jiang, W. Peng, and J. Wang, "Influence of hole geometry on film cooling effectiveness for a constant exit flow area," *Applied Thermal Engineering*, vol. 130, 2018.